A Preliminary Survey of Radio-Frequency Interference over the U. S. in Aqua AMSR-E Data

L. Li[1], E. Njoku[1], E. Im[1], P. Chang[2], K. St.Germain[3]

[1]Jet Propulsion Laboratory
California Institute of Technology
Pasadena, California 91109

[2]National Oceanic and Atmospheric Administration
NESDIS Office of Research and Applications
Camp Springs, MD 20746

[3]Naval Research Laboratory
Microwave Remote Sensing Section
Remote Sensing Division
Washington DC 20375

Accepted for publication in
IEEE Transactions on Geoscience and Remote Sensing

Corresponding Author: Li Li
Jet Propulsion Laboratory
Mail Stop: 300-243
4800 Oak Grove Drive
Pasadena, CA 91109

ABSTRACT

A spectral difference method is used to quantify the magnitude and extent of radio-frequency interference (RFI) observed over the U. S. in the Aqua AMSR-E radiometer channels. A survey using data from the AMSR-E instrument launched in May 2002 shows the interference to be widespread in the C-band (6.9 GHz) channels. The RFI is located mostly, but not always, near large highly populated urban areas. The locations of interference are persistent in time, but the magnitudes show temporal and directional variability. Strong and moderate RFI can be identified relatively easily using an RFI index derived from the spectral difference between the 6.9 and 10.7 GHz channels. Weak RFI is difficult to distinguish however from natural geophysical variability. These findings have implications for future microwave sensing at C-band, particularly over land areas. An innovative concept for radiometer system design is also discussed as a possible mitigation approach.

I. Introduction

The Advanced Microwave Scanning Radiometer (AMSR-E) [1] was developed by the National Space Development Agency of Japan (NASDA) and launched on board the National Aeronautics and Space Administration (NASA) EOS Aqua satellite on May 4, 2002. A sister instrument, the AMSR [2] on the Japanese ADEOS-II satellite, is scheduled for launch in December 2002. The Naval Research Laboratory's WindSat radiometer [3] on the Coriolis satellite arel also launched in January 2003. The AMSRs and WindSat are functionally quite similar in terms of frequencies, viewing configurations, and spatial resolutions to the Conical Microwave Imager/Sounder (CMIS) [4] planned for launch as part of the National Polar-orbiting Operational Environmental Satellite System (NPOESS) in the 2008-2009 time frame. All these sensors have dual-polarized channels near 6.9, 10.8, and 18.7 GHz for ocean and land surface sensing applications. Analyses of data from the AMSR-E, AMSR, and WindSat sensors will provide opportunities for evaluating the CMIS design and expected performance.

Early examinations of AMSR-E instrument data have shown evidence of extensive Radio-Frequency Interference (RFI) in the 6.9-GHz brightness temperature measurements. As part of the evaluation team activities, this paper provides a preliminary analysis of the magnitude and extent of the interference. Our primary objective is to identify, survey, and quantify the RFI, globally and in regions where the problem appears most severe such as the U. S. The study results will provide useful information on the utility of the 6.9-GHz channels of AMSR-E, AMSR, and WindSat data for land surface studies (in particular for soil moisture sensing), and will indicate potential problems and directions for improvement in the future CMIS radiometer.

II. AMSR-E Description

The AMSR-E instrument, developed by NASDA, follows the heritage of spaceborne imaging radiometers including the Scanning Multichannel Microwave Radiometer (SMMR) [5], the Special Sensor Microwave/Imager (SSM/I) [6] and the Tropical Rainfall Measuring Mission (TRMM) Microwave Imager (TMI) [7]. AMSR-E makes dual-polarized passive microwave measurements at six frequencies: 6.9, 10.7, 18.7, 36.5, and 89 GHz. From the 705-km Aqua orbit the antenna nadir angle of 47.4^{o} provides an Earth incidence angle of 55^{o}. The antenna beams scan conically about the nadir axis. The $\pm 61^{o}$ active portion of the azimuth scan angle provides an observation swath width of 1445 km. The orbit is Sun-synchronous with equator crossings at 1:30 pm and 1:30 am local solar time. Additional details of the radiometer and antenna characteristics are listed in Table I.

The AMSR-E Level 1A data are generated at the NASDA Earth Observation Center (EOC) in Japan. The Level 1A data contain sensor counts and coefficients needed to compute antenna temperatures and, subsequently, surface brightness temperatures at level 1B. The level 1A data are sent to the Physical Oceanography Distributed Active Archive Center (PO.DAAC) located at the Jet Propulsion Laboratory in Pasadena, California. From there the data are transmitted to the U. S. AMSR-E Science Information Processing System (SIPS). The SIPS has two components, one located at the Remote Sensing Systems (RSS) facility in Santa Rosa, CA, and the other at the

Global Hydrology and Climate Center (GHCC) in Huntsville, AL. At the RSS SIPS, Level 2A brightness temperatures are generated by reconstructing the AMSR-E antenna gain patterns at each channel to five footprints, corresponding to the footprint sizes of the 6.9, 10.7, 18.7, 36.5 and 89 GHz observations [8]. The sampling intervals are approximately 10 km for the four low resolutions, and 5 km for the highest resolutions. The level 2A data contain as a subset the level 1B data. The Level 2A data are sent to the GHCC SIPS for higher-level processing. The data products are subsequently transferred to the National Snow and Ice Data Center (NSIDC) DAAC in Boulder, CO for archiving and distribution.

III. RFI AND NATURAL EMISSION CHARACTERISTICS

Microwave radiometers are sensitive devices designed to measure relatively weak naturally-emitted thermal radiation over broad spectral bands. Man-made emissions from active microwave transmitters are distinctly different from those of natural sources in terms of intensity, spatial variability, polarization and spectral characteristics. Although typically narrowband, these signals have high power levels that can cause spurious measurements and saturate a radiometer receiver if the transmissions fall within its measurement frequency band. From a radiometric point of view these interfering sources are classed as radio-frequency interference or RFI. RFI signals typically originate from coherent point targets, i.e., radiating devices and antennas. Their power levels are several orders of magnitude higher than natural thermal emissions, and are often directional and can be either continuous or intermittent. RFI originates from a wide variety of sources, typically clustered near highly populated areas and centers of technical and industrial activity.

The World Radiocommunication Conferences recommend allocations of the radio frequency spectrum for various services, including passive services such as passive Earth exploration satellites and radio astronomy. These allocations are documented internationally by the Radio Regulations of the International Telecommunications Union [9]. Within the U.S., the Office of Spectrum Management of the National Telecommunications and Information Administration (NTIA) has responsibility for spectrum management. Table 2 shows the spectrum allocations at the AMSR-E frequencies as listed by the NTIA (http://www.ntia.doc.gov/osmhome/redbook/redbook.html). Near 7 GHz, the "Fixed" and "Mobile" radio services, including cable TV relay and auxiliary broadcasting, are the major sources of RFI for spaceborne radiometry. The actual sources and characteristics of RFI can only be determined by measuring the radio spectrum in this frequency band at the RFI contamination sites.

Natural radiation emitted by the Earth's surface and atmosphere has characteristics that are very different than RFI. The radiation is spatially distributed and consists of broadband incoherent microwave emissions. At the AMSR-E low-frequency channels the atmosphere is relatively transparent and the polarization and spectral characteristics of the received microwave radiation are dominated by emission and scattering at the surface. Over land, the emission and scattering depend primarily on the water content of the soil, the surface roughness and topography, the surface temperature, and the vegetation cover [10]. The surface brightness

temperatures tend to increase with frequency (positive spectral gradient) due to the absorptive effects of water in soil and vegetation that also increase with frequency. However, as the frequency increases, scattering effects from the surface and vegetation also increase, acting as a factor to reduce the brightness temperatures. When volume scattering effects dominate, the brightness temperature spectrum can become flat or even have a negative gradient, i.e., the AMSR-E brightness temperature at 10.7 GHz can be lower than at 6.9 GHz. However, at frequencies below 30 GHz scattering effects are usually limited, and such brightness temperature spectral decreases are moderate at most. RFI at C-band is the only possible cause for the brightness temperature at 6.9 GHz to be significantly higher than at 10.7 GHz. Thus, large positive differences obtained by subtracting the 10.7-GHz brightness temperatures from the 6.9-GHz brightness temperatures (negative spectral gradients) can be used to separate RFI at 6.9 GHz from the natural emission background. In this paper we examined primarily the low frequency AMSR-E channels (18 GHz and lower) over soil and vegetated land surfaces. It should be noted that scattering signatures can be much stronger for other surfaces such as dry snow, ice and some desert surfaces. In these cases, the spectral gradient may not be a good indicator of RFI.

IV. RFI IDENTIFICATION

Fig. 1 shows an example of the horizontally polarized AMSR-E brightness temperatures at 6.9, 10.7, and 18.7 GHz for a descending pass over the United States. For simplicity, the 6.9, 10.7 and 18.7 GHz channels and measurements are designated by 7, 10 and 18 GHz, respectively, in all figures. Consistent spatial patterns of natural brightness temperature variability are visible in all the channels. In the 6.9 GHz image however there are several visible "hot spots" where the brightness temperatures far exceed feasible levels for naturally-emitted radiation. These are potential locations of RFI. To examine the RFI and spectral characteristics in detail, we sub-sampled the AMSR-E data in the along track direction, as indicated by the white line near the center of the swath in Fig. 1. The largest RFI hot spot along this line is located at Denver, Colorado. Fig. 2 plots sequentially the sub-sampled brightness temperatures (TBs) at both polarizations V and H, and the polarization difference ($TB_V - TB_H$). The sudden drop of the brightness temperature at 6.9 GHz to 0 K is caused by the data processing procedure used by NASDA and RSS. The Level 1B processing resets the brightness temperatures to 0 K when they are larger than a 370 K threshold. The Level 2A processing resets the brightness temperatures to 0 K at a 330 K threshold. These different threshold values contribute to the discrepancy between Level 1B and Level 2A data statistics. Apart from the 6.9-GHz channels, the brightness temperatures in all other channels vary quite smoothly and are well correlated with each other. In the 6.9-GHz channels several RFI spikes are observed. Where the spike peaks are very high (> 330 K), such as at points A, B and D, there is a positive identification of RFI. The brightness temperatures at C and E are also likely to be RFI-contaminated due to their high spatial frequency and decorrelation with the other channels. At point A, the polarization difference spikes upward, suggesting that the RFI source at this point is mostly vertically polarized. The downward spike of the polarization difference at point B suggests a mostly horizontally polarized RFI source.

To examine the spectral signatures, we plotted the spectral differences of the sub-sampled brightness temperatures in Fig. 3 for both vertical and horizontal polarizations. When compared with Fig. 2 over the land region, it is clear that the RFI at 6.9 GHz is delineated best by the negative spectral gradients between 6.9 and 10.7 GHz (i.e., TB_{10V}–TB_{7V} and TB_{10H}–TB_{7H}), which can have magnitudes as large as 100 K. For the vertical polarization (top panel), strong RFI can be classed as (TB_{10V}–TB_{7V}) < –10 K, and moderate RFI as –10 K < (TB_{10V}–TB_{7V}) < –5 K. The horizontal polarization data can be similarly classed. Based on this observation, we have used the negative spectral difference as an RFI Index (RI). i.e., the RI at 6.9 GHz for polarization *p* is:

$$RI_{7p} = TB_{7p} - TB_{10p} \quad (1)$$

This RFI index can be used not only to identify the location of RFI but also to quantify its intensity. The larger the RI, the stronger the RFI. Note that a slightly negative RI does not necessarily suggest that the region is RFI-free, since the RFI-free TB_{10p} is intrinsically higher than the RFI-free TB_{7p} (i.e., negative gradient). Weak RFI could increase RI slightly, but not enough to make it positive.

Once a location of RFI has been identified, its polarization characteristics can be calculated using an RFI Polarization Index (RPI), i.e.:

$$RPI = (RI_V - RI_H) / (RI_V + RI_H) \quad (2)$$

RPI = 1 for vertically polarized RFI, and RPI = –1 for horizontally polarized RFI.

To demonstrate the effectiveness of the spectral gradient in separating RFI from the natural surface background, the RI histogram for the 6.9 GHz vertical polarization (TB_{7V}–TB_{10V}) is shown in Fig. 4. There are three peaks near RI = –12 K, –4 K and 1 K. The peak near –12 K represents the ocean signature. The peak near –4 K represents mostly land emission. The third peak consists of a mixture of land and RFI-contaminated land observations. These can be seen clearly with the RI map in Fig. 5, which partitions the brightness temperatures into three RI intervals: (a) –5 K < RI < 5 K contains both weak RFI and RFI-free land pixels. Most RFI-free observations are in the negative part of this range. (b) 5K < RI < 10K contains moderate RFI. (c) RI > 10 contains strong RFI. Note that in case (a) it may be quite difficult to separate weak RFI from the natural signal. Figure 6 shows an example of an RFI Polarization Index (RPI) map based on one AMSR-E descending pass. It can be seen that the RPI is mostly close to zero, suggesting that the RFI does not appear to favor the vertical or horizontal polarizations, although they should be coherent and polarized. For a few locations in Texas, South Dakota and Montana, the RFI is vertically polarized.

We would like to emphasize that the Level 1B and 2A data used here were experimental release of AMSR-E products. The brightness temperatures were not yet fully calibrated at the time of this study. Therefore the thresholds presented here are likely to change once the AMSR-E data are well calibrated and formally released.

V. RFI Surveys Over North and Central America

A survey of RFI over North and Central America was generated by processing and merging multiple swaths of AMSR-E data for both vertical and horizontal polarizations. The merged ascending pass swath data for the U.S. are shown in the two panels of Fig. 7 for V and H polarizations. For reference, in the lower panel the locations of U.S. cities with populations above 100,000 have been indicated by asterisks (*). It is to be noted that the city locations were extracted from the United Nation database, which many contains errors in city population and city latitude and longitude. Descending passes were shown in the two panels of Fig. 8. These maps are useful for understanding RFI spatial and temporal variations and investigating the sources and spectra. Several distinct features are visible from the maps.

(1) In North and Central America, the RFI is confined mostly within the continental U.S. There is very little RFI in Canada and Mexico.
(2) The RFI occurs mostly at or near major U.S. cities or airports, with some exceptions. Some RFI can be distinguished along major highways. The possible RFI sources include, but are not limited to, facilities for cable TV relay, wireless communication, airport radar, and manufacturing operations, etc.
(3) Most RFI does not appear to favor vertical or horizontal polarizations, with some exceptions.
(4) The RFI intensities are stronger for ascending (near 1:30 pm) than for descending passes (near 1:30 a.m.), which may reflect differences in human activity patterns between day and night. Also, differences in RFI between ascending and descending passes may be due to differences in the AMSR-E antenna azimuth viewing direction of RFI sources.

More detailed regional maps were generated to focus on specific AMSR-E targets of interest, in particular the planned U.S. soil moisture validation sites [1]. Fig. 9 shows RFI maps for the regions of (a) Iowa, (b) Oklahoma, and (c) Alabama/Georgia. Cities with populations above 100,000 are indicated by asterisks. In Fig 9(a) there is widespread RFI evident in the neighborhoods of Des Moines, Cedar Rapids, and Sioux Falls, though not centered directly on those cities. Surprisingly there is no RFI near Madison and Lincoln despite the sizeable population and urbanization of these cities. Additional investigations need to be undertaken using ground-based RFI detectors to locate and characterize the specific sources of the RFI.

VI. An Innovative Concept for Radiometer System Design And RFI Suppression Technique

This RFI contamination problem will profoundly compromise the science objectives of AMSR-E, as well as its sister instrument, AMSR-A, on the Japan's ADEOS-2 satellite. If not properly corrected, the science value of spaceborne radiometers for many other missions, including the Navy WindSat and NPOESS CMIS will be drastically reduced. All of these missions have included C-band channels to enhance their land and ocean surface sensing capabilities, especially the soil moisture monitoring capability from space, which is one of the

top science priorities for NASA and NPOESS for the next decade. To preserve those science objectives, some RFI mitigation approaches have to be developed.

Although RFI Contamination is an emerging challenge for spaceborne radiometry, it has been a well-known problem for active sensors for years. Over the last decade, many RFI suppression technologies have been developed successfully for ultra wide-band radar systems [11]. Those technologies can be adopted for radiometry with certain modifications to the radiometer system design, which can be understood through following comparisons between active and passive sensors.

Active sensors transmit coherent signals and perform coherent processing on the received backscattering signals, which have both coherent and incoherent components. The RFI is imposed on the coherent component with different spectrum signatures. Because coherent detection is used in active sensor, we can transform the received signals into frequency domain and filter out the RFI coherently and adaptively by seeking zero correlation between RFI and natural targets while minimizing the RFI prediction error.

In a conventional radiometer, a square-law detector is often used to measure the total power received, which is an irreversible process in which the nature radiation and RFI are summed together and cannot be separated. Furthermore, for dual polarization measurements, because the phase information is discarded at the very beginning of data processing no spectrum information can be collected, and therefore RFI cannot be removed coherently in the spectrum domain. However, RFI removal capability can be added easily by replacing the square-law detector with a high-performance A/D converter and an on-board data processor. With the emergence of wideband, high dynamic range A/D converters, it is straightforward to implement such a new concept for radiometry. Once the spectra of the received signals are sampled coherently, the active RFI suppression technique can be adopted to remove the coherent part of the spectra from the incoherent thermal noise (Brightness temperature) background. Obviously the sampled spectra are also useful in collecting and studying the RFI sources and its signatures, which is essential in developing RFI suppression algorithms. In addition, the RFI suppression algorithm can be performed on-board, in real-time and updated throughout the mission by using the FPGA-based programmable processing technology.

VII. Discussion

In this paper we have examined only RFI over land. This does not necessarily suggest that there is no RFI over ocean regions, only that our first priority has been to examine the distribution of major RFI sources over land and their impact for land remote sensing. Also, we have analyzed primarily data over the United States since our preliminary survey indicated that this was the region with the most widespread and severe RFI. In subsequent studies the RFI over other land regions and ocean regions will be examined also.

ACKNOWLEDGMENTS

This research is supported jointly by the EOS Aqua Algorithm and Validation Program of NASA, and the NOAA NPOESS Integrated Program Office under the contract with NOAA/NESDIS/ORA. The data are made available as part of the NASDA/NASA AMSR-E team activities, and were accessed through the AMSR-E SIPS facility at NASA/MSFC. This research was carried out in part at the Jet Propulsion Laboratory, California Institute of Technology, under contract with the National Aeronautics and Space Administration.

REFERENCES

[1] Spencer, R., F. Wentz, C. Kummerow, T. Wilheit, R. Ferraro, D. Cavalieri, J. Comiso, A. Chang, and E. Njoku, AMSR-E Science data validation plan. Available at http://eospso.gsfc.nasa.gov/validation/pmval.html.

[2] Imaoka, K., T. Sezai, T. Takeshima, T. Kawanish, and A. Shibata, "Instrument characteristics and calibration of AMSR and AMSR-E," *Proceedings of Int. Geoscience and Remote Sensing Symposium*, Toronto, Canada, June 2002.

[3] Gaiser, P.W., and K.M. St. Germain, "Spaceborne polarimetric microwave radiometry and the Coriolis WindSat system," *IEEE Aerospace Conference Proceedings*, Vol. 5, 159 –164, 2000.

[4] Kunkee, D.B., N.S. Chauhan, and J.J. Jewell, "Phase one development of the NPOESS Conical-scanning Microwave Imager/Sounder," Proceedings of Int. Geoscience and Remote Sensing Symposium, Toronto, Canada, June 2002.

[5] Njoku, E., J.M. Stacey, and F.T. Barath, "The SEASAT scanning multichannel microwave radiometer (SMMR): Instrument description and performance," *IEEE J. Oceanic Engineering*, vol. 5, pp. 100-115, 1980.

[6] Hollinger, J.P., J.L. Peirce, and G.A. Poe, "SSM/I instrument evaluation," *IEEE Trans. Geosci. Rem. Sens.*, vol. 28, pp. 781-790, 1990.

[7] Kummerow C, Simpson J, Thiele O, Barnes W, Chang ATC, Stocker E, Adler RF, Hou A, Kakar R, Wentz F, Ashcroft P, Kozu T, Hong Y, Okamoto K, Iguchi T, Kuroiwa H, Im E, Haddad Z, Huffman G, Ferrier B, Olson WS, Zipser E, E.A. Smith, T. Wilheit, G. North, T. Krishnamurti, K. Nakamura, " The status of the Tropical Rainfall Measuring Mission (TRMM) after two years in orbit", *J. Applied Meteorology* ,39, (12), 1965-1982, 2000.

[8] P. Ashcroft and F. Wentz, *Algorithm Theoretical Basis Document, AMSR Level 2A Algorithm*, RSS Tech. Report 121599B-1, Remote Sensing Systems, Santa Rosa, CA, November, 2000, http://eospso.gsfc.nasa.gov/atbd/pg1.html.

[9] ITU, *Radio Regulations*, International Telecommunications Union, Geneva, Switzerland, 2001.

[10] E. G. Njoku and L. Li, "Retrieval of land surface parameters using passive microwave measurements at 6-18 GHz," *IEEE Trans. Geosci. Rem. Sens.*, vol. 37, pp. 79-93, 1999.

[11] Miller, T., L. Potter, and J. McCorkle, " RFI Suppression for Ultra Wideband Radar", *IEEE Transactions on Aerospace and Electronic Systems*, vol. 33, pp. 1142-1156, 1997.

Table I. AMSR-E Characteristics

Center frequencies (GHz)	**6.925**	**10.65**	**18.7**	**23.8**	**36.5**	**89.0**
Bandwidth (MHz)	350	100	200	400	1000	3000
Sensitivity (K)	0.3	0.6	0.6	0.6	0.6	1.1
Instantaneous FOV (km)	75x43	48x27	27x16	31x18	14x8	6x4
Sampling interval (km)	10x10	10x10	10x10	10x10	10x10	5x5
Integration time (msec)	2.6	2.6	2.6	2.6	2.6	1.3
Main beam efficiency (%)	95.3	95.0	96.3	96.4	95.3	96.0
Beamwidth (half-power, degrees)	2.2	1.4	0.8	0.9	0.4	0.18

Table II. Radio Frequency Allocation.

Frequency (GHz)	United States	International	Remarks
6.7–7.2	FIXED FIXED-SATELLITE (Earth-to-space) MOBILE SPACE RESEARCH (Earth-to-space)	FIXED FIXED-SATELLITE (Earth-to-space, Space-to-Earth) MOBILE	Auxiliary Broadcasting Cable TV Relay
10.6–10.7	EARTH EXPLORATION-SATELLITE (passive) SPACE RESEARCH (passive) RADIO ASTRONOMY	EARTH EXPLORATION-SATELLITE (passive) SPACE RESEARCH (passive) RADIO ASTRONOMY MOBILE	Fixed Microwave
18.6–18.8	EARTH EXPLORATION-SATELLITE (passive) FIXED-SATELLITE (Earth-to-space) SPACE RESEARCH (passive)	EARTH EXPLORATION-SATELLITE (passive) FIXED-SATELLITE (space-to-Earth) FIXED MOBILE	Satellite Communication
23.6–24.0	EARTH EXPLORATION-SATELLITE (passive) RADIO ASTRONOMY SPACE RESEARCH (passive)	EARTH EXPLORATION-SATELLITE (passive) RADIO ASTRONOMY	
36.0–37.0	EARTH EXPLORATION-SATELLITE (passive) SPACE RESEARCH (passive) FIXED MOBILE	EARTH EXPLORATION-SATELLITE (passive) SPACE RESEARCH (passive) FIXED MOBILE	
86.0–92.0	EARTH EXPLORATION-SATELLITE (passive) RADIO ASTRONOMY SPACE RESEARCH (passive)	EARTH EXPLORATION-SATELLITE (passive) RADIO ASTRONOMY SPACE RESEARCH (passive)	

LIST OF FIGURES

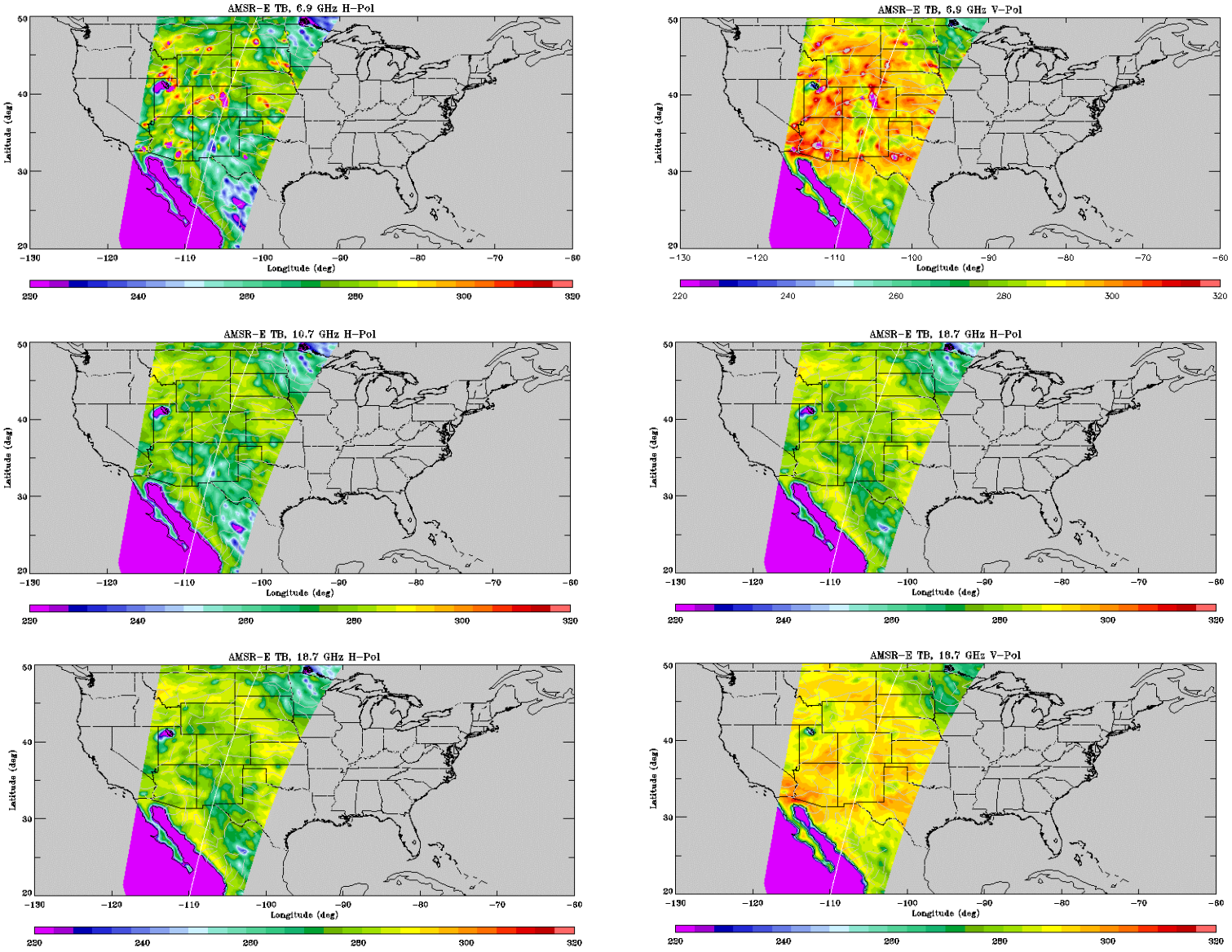
AMSR-E TB, 6.9 GHz H-Pol
AMSR-E TB, 6.9 GHz V-Pol
AMSR-E TB, 10.7 GHz H-Pol
AMSR-E TB, 18.7 GHz H-Pol
AMSR-E TB, 18.7 GHz H-Pol
AMSR-E TB, 18.7 GHz V-Pol
Latitude (deg)
Longitude (deg)
50
40
30
20
-130
-120
-110
-100
-90
-80
-70
-60
220
240
260
280
300
320

Figure 1

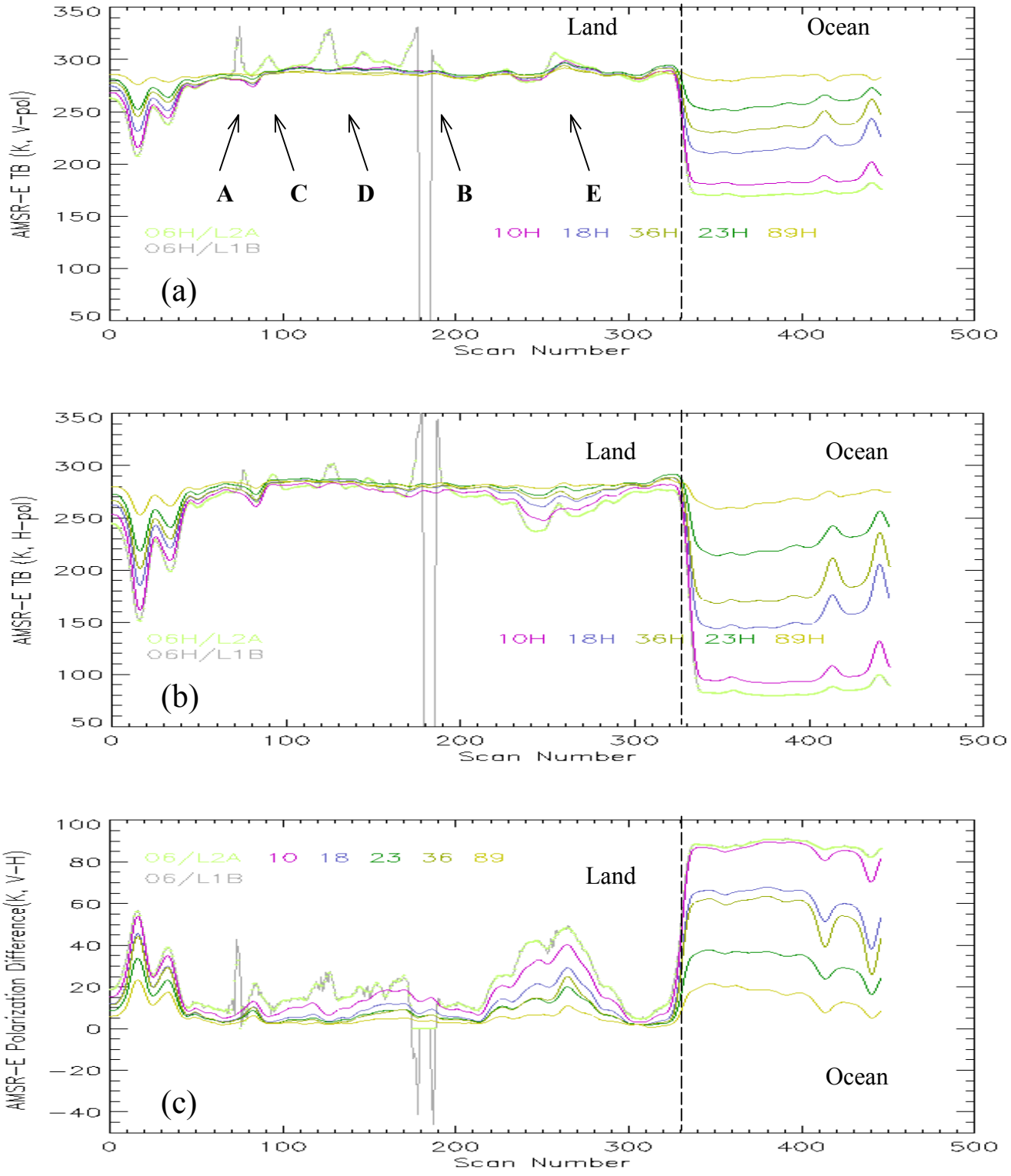
AMSR-E TB (K, V-pol)
Land
Ocean
A
C
D
B
E
06H/L2A
06H/L1B
10H 18H 36H 23H 89H
(a)
Scan Number
AMSR-E TB (K, H-pol)
Land
Ocean
06H/L2A
06H/L1B
10H 18H 36H 23H 89H
(b)
Scan Number
AMSR-E Polarization Difference(K, V-H)
06/L2A 10 18 23 36 89
06/L1B
Land
Ocean
(c)
Scan Number

Figure 2

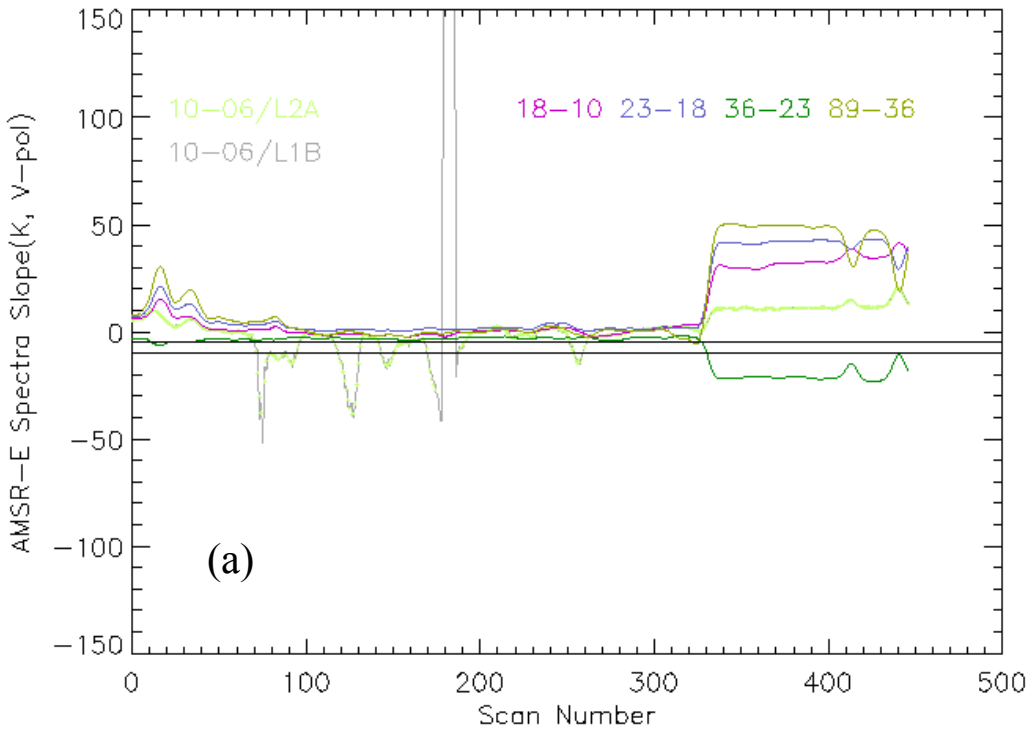
10–06/L2A
10–06/L1B
18–10 23–18 36–23 89–36
AMSR–E Spectra Slope(K, V–pol)
Scan Number
(a)

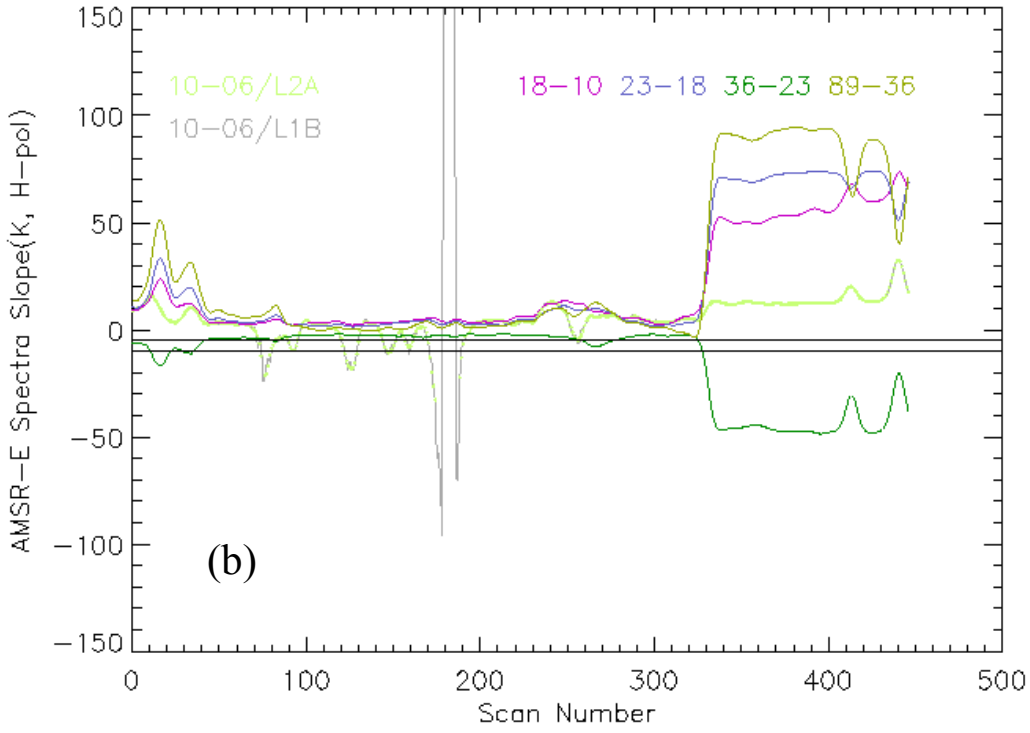
10–06/L2A
10–06/L1B
18–10 23–18 36–23 89–36
AMSR–E Spectra Slope(K, H–pol)
Scan Number
(b)

Figure 3

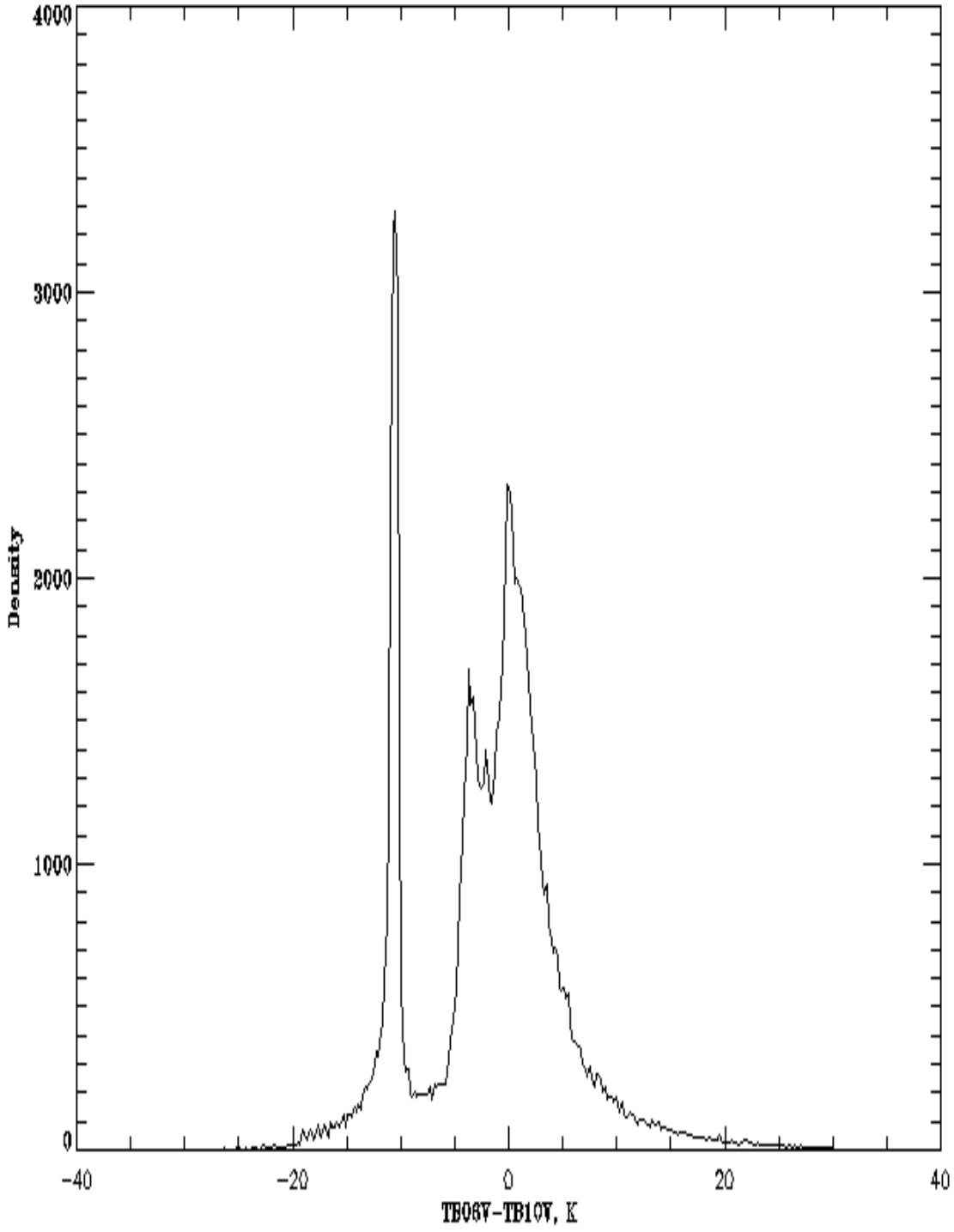

Figure 4

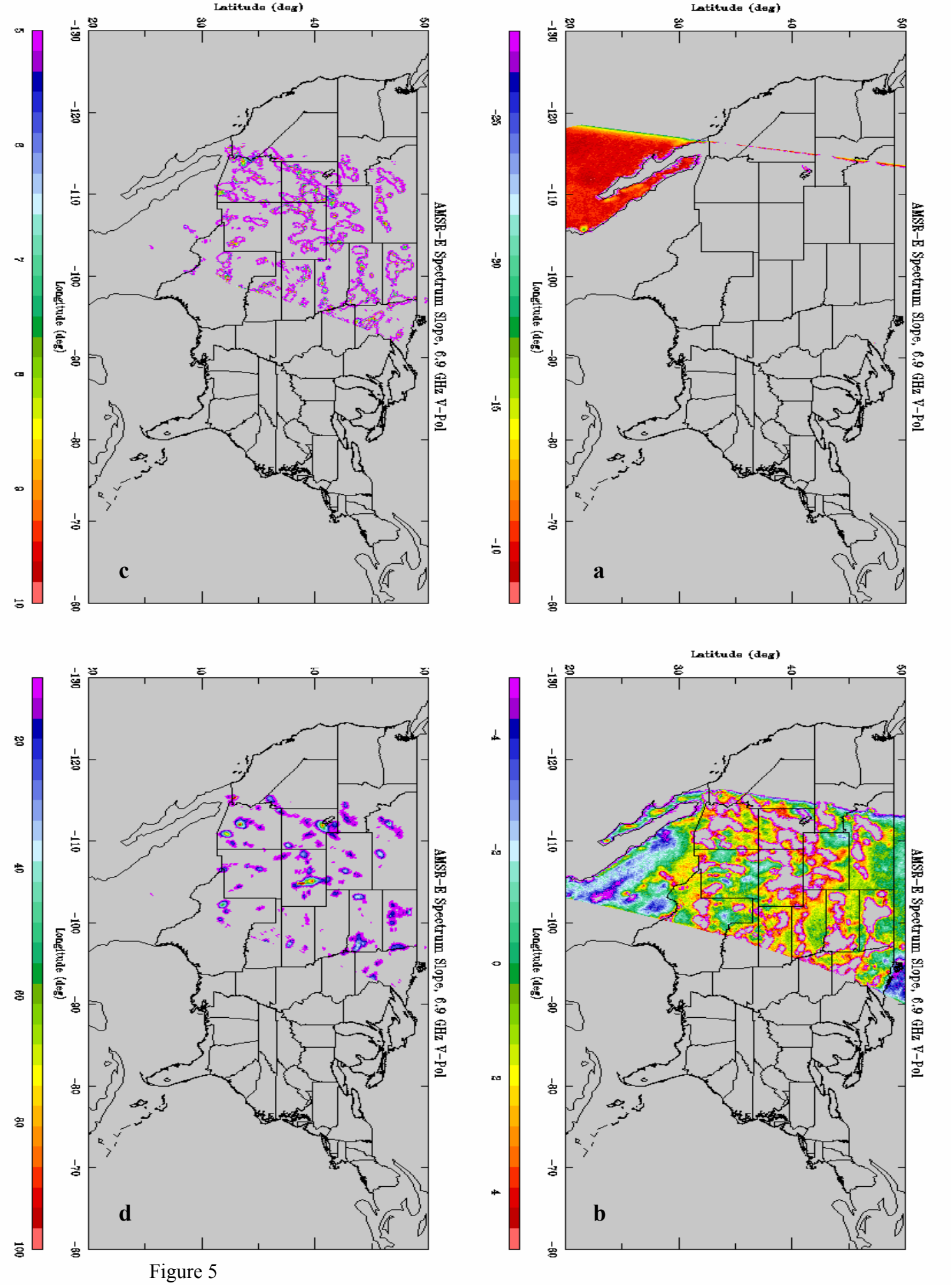
AMSR-E Spectrum Slope, 6.9 GHz V-Pol
Latitude (deg)
Longitude (deg)
a
b
c
d

Figure 5

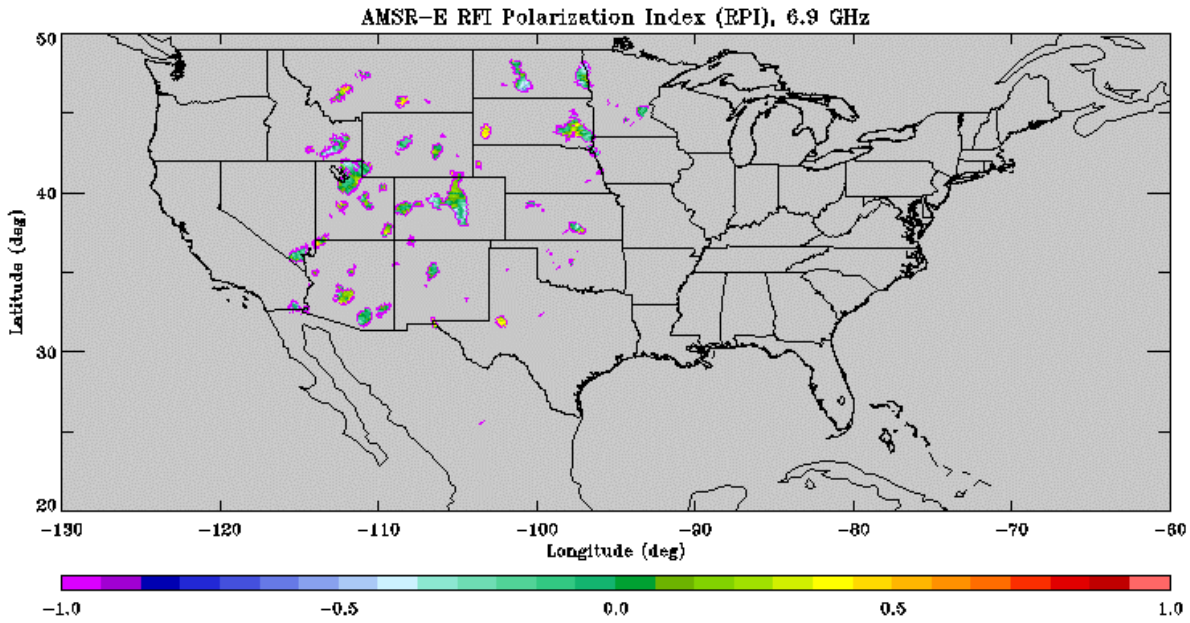
AMSR-E RFI Polarization Index (RPI), 6.9 GHz
50
40
30
20
Latitude (deg)
-130
-120
-110
-100
-90
-80
-70
-60
Longitude (deg)
-1.0
-0.5
0.0
0.5
1.0

Figure 6

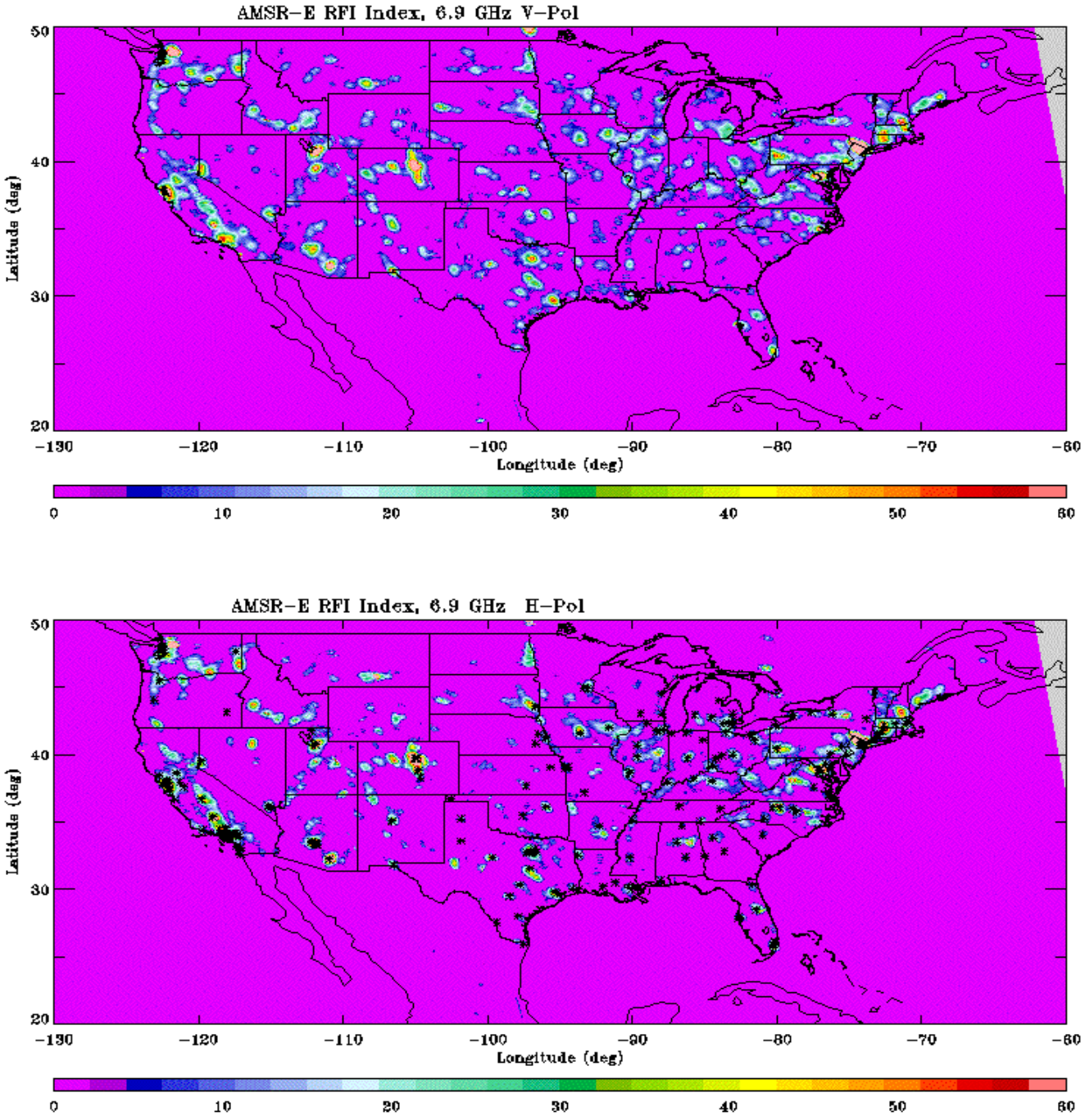
AMSR-E RFI Index, 6.9 GHz V-Pol
Latitude (deg)
50
40
30
20
-130
-120
-110
-100
-90
-80
-70
-60
Longitude (deg)
0
10
20
30
40
50
60
AMSR-E RFI Index, 6.9 GHz H-Pol
Latitude (deg)
50
40
30
20
-130
-120
-110
-100
-90
-80
-70
-60
Longitude (deg)
0
10
20
30
40
50
60

Figure 7

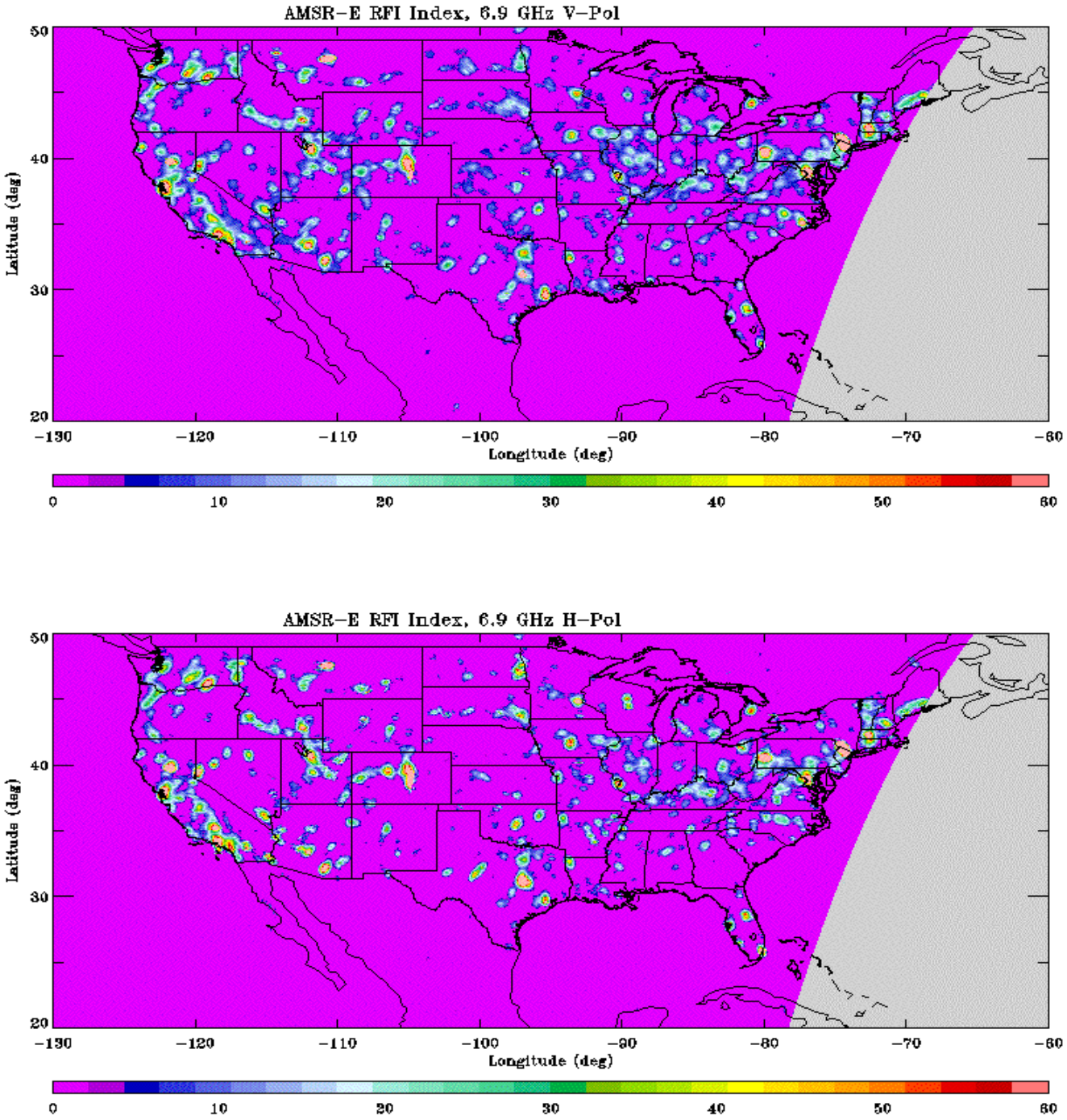
AMSR-E RFI Index, 6.9 GHz V-Pol
Latitude (deg)
50
40
30
20
-130
-120
-110
-100
-90
-80
-70
-60
Longitude (deg)
0
10
20
30
40
50
60
AMSR-E RFI Index, 6.9 GHz H-Pol
Latitude (deg)
50
40
30
20
-130
-120
-110
-100
-90
-80
-70
-60
Longitude (deg)
0
10
20
30
40
50
60

Figure 8

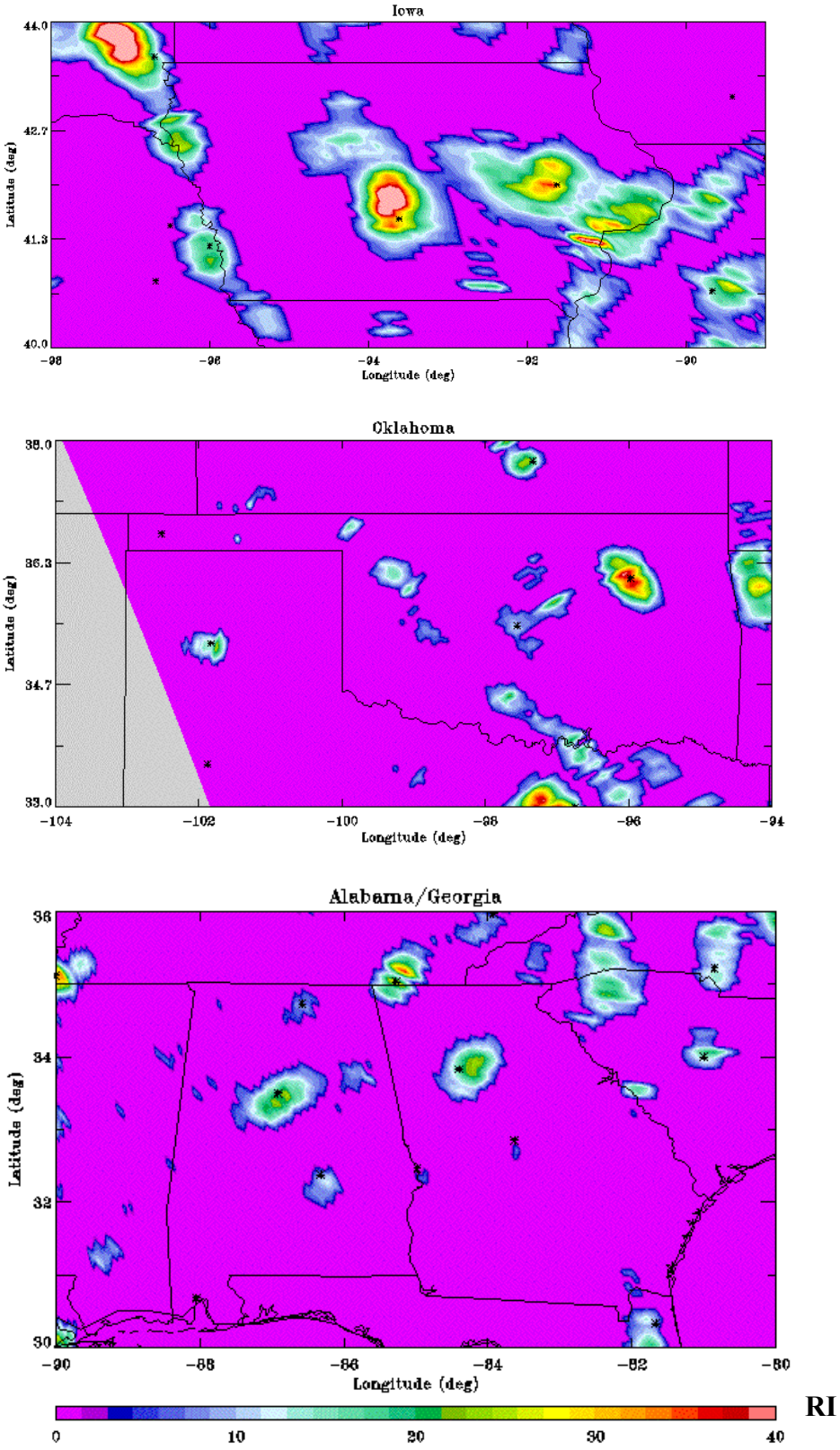
Iowa
Latitude (deg)
Longitude (deg)
Oklahoma
Latitude (deg)
Longitude (deg)
Alabama/Georgia
Latitude (deg)
Longitude (deg)
RI
0
10
20
30
40

Figure 9